

GaussianHead: Impressive Head Avatars with Learnable Gaussian Diffusion

Jie Wang¹, Jiu-Cheng Xie¹, Xianyan Li¹, Feng Xu², Chi-Man Pun³, Hao Gao^{1*}

¹Nanjing University of Posts and Telecommunications

²Tsinghua University

³University of Macau

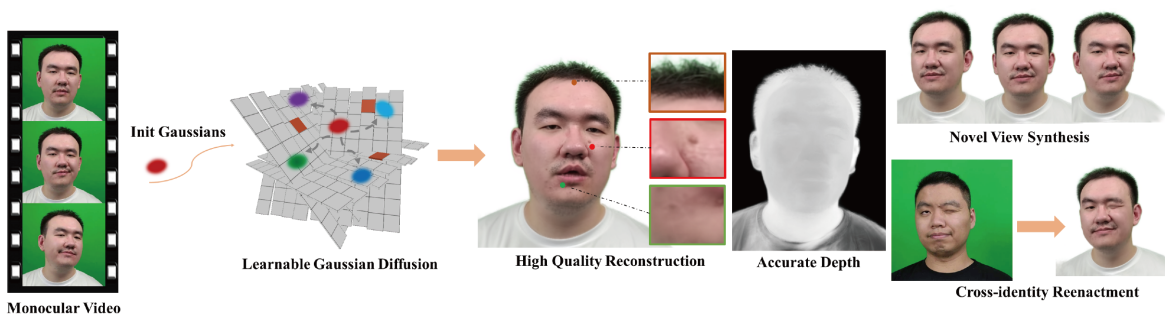


Figure 1: GaussianHead is trained on monocular video using geometric primitives that are randomly initialized anisotropic 3D Gaussians. Through diffusion of the core Gaussian, it learns canonical features that act as generation conditions for semantic information (opacity and color), leading to a fully distorted factor plane entry-wise. GaussianHead demonstrates outstanding performance in mainstream tasks.

Abstract

Previous head avatar methods have primarily relied on fixed-shape scene primitives, lacking a balance between geometric topology, texture details, and computational efficiency. Some hybrid neural network methods (e.g., planes and voxels) gained advantages in fast rendering, but they all used axis-aligned mappings to extract features explicitly, leading to issues of axis-aligned bias and feature dilution. We present GaussianHead, which utilizes deformable 3D Gaussians as building blocks for the head avatars. We propose a novel methodology where the core Gaussians designated for rendering undergo dynamic diffusion before being mapped onto a factor plane to acquire canonical sub-factors. Through our factor blending strategy, the canonical features for the core Gaussians used in rendering are obtained. This approach deviates from the previous practice of utilizing axis-aligned mappings, especially improving the representation capability of subtle structures such as teeth, wrinkles, hair, and even facial pores. In comparison to state-of-the-art methods, our unique primitive selection and factor decomposition in GaussianHead deliver superior visual results while maintaining rendering performance (0.1 seconds per frame). Code will be released for research: <https://github.com/chiehwangs/gaussian-head>

chiehwangs/gaussian-head

1 Introduction

Creating personalized avatars for everyone is essential for the future wide-ranging applications of virtual reality. Early head avatars focused on coarse-skinned surfaces. They mostly created surface templates for head avatars without details, based on face data obtained from extensive scans[Cao *et al.*, 2013; Li *et al.*, 2017; Gerig *et al.*, 2018]. Building implicit head avatars using Signed Distance Fields (SDF)[Yariv *et al.*, 2021; Yariv *et al.*, 2020] helped overcome the deficiencies of skinned models and achieved better head geometry[Zheng *et al.*, 2022]. Nevertheless, implicit surfaces lacked excellent expressive power for fine structures and fast rendering. With the rise of neural radiance fields (NeRF[Mildenhall *et al.*, 2021]), combining explicit data structures to build volumetric neural radiance fields is a current trend. [Müller *et al.*, 2022; Fridovich-Keil *et al.*, 2023; Cao and Johnson, 2023; Chan *et al.*, 2022; Chen *et al.*, 2022] store scenes using explicit data containers, allowing the use of smaller MLPs to focus on decoding semantic information (i.e., density and color), resulting in faster optimization speed. Methods like [Xu *et al.*, 2023a; Gao *et al.*, 2022; Tang *et al.*, 2022; Li *et al.*, 2023] achieved realistic head avatars by storing scenes using voxels or multiple 2D planes instead of the weights of neural networks, but these methods are limited by the resolution constraints associated with explicit structures, along with the deficiencies introduced by feature bias and di-

*Corresponding author.

	Fast Rendering	Easy Animation	Flexible Primitives	Explicit Geometry	Subtle Texture
Meshe	✓	✓	✗	✓	✗
Points	✓	✓	✗	✓	✓
Volumetric NeRF	✓	✗	✗	✗	✓
Implicit Surface	✗	✗	✗	✓	✗
3D Gaussians (Ours)	✓	✓	✓	✓	✓

Table 1: GaussianHead is easy to integrate with existing hardware to achieve fast rendering and can flexibly represent even hair-like or teech structures. It also features deformable primitives to represent complex structures with fewer elements.

lution resulting from axis-aligned mappings. Therefore, they predominantly manifest visual effects such as “smoothing” and “blurring.”

In this paper, we employ pre-retrieved facial expression parameters as conditions to transform randomly initialized 3D Gaussians into canonical space to address dynamic facial movements. To simultaneously capture complex facial muscle dynamics and intricate textures, we utilize an explicit data container—a parameterized tri-plane—to access the canonical features of Gaussians and use them to obtain Gaussian attributes for rendering. However, directly projecting 3D primitives onto a 2D plane through axis-aligned mapping introduces axis-aligned bias in features[Zhang *et al.*, 2012; Yi *et al.*, 2023]. Additionally, primitives projected along the same mapping line dilute each other’s features stored on the plane, a phenomenon exacerbated in complex structures due to increased overlap. Therefore, we propose a dynamic diffusion strategy for 3D Gaussians.

For each 3D Gaussian in the canonical space, we treat it as a core Gaussian and subject it to multiple diffusions using sets of learnable quaternions. The resulting diffused Gaussians are referred to as “sub-Gaussians.” These sub-Gaussians are further mapped onto factor planes to extract their respective factors. We propose a multi-resolution factor integration approach to generate canonical features that more accurately represent complex regions. Canonical features are used to decode the opacity and view-dependent spherical harmonic coefficients of 3D Gaussians. Finally, a differentiable gaussian rasterizer is employed to render realistic head avatars. Refer to Figure. 2 for an overview of our approach.

In summary, our contributions are as follows:

- Leveraging anisotropic 3D Gaussian primitives and explicit parameterized tri-plane to construct dynamic head avatars, enabling high-fidelity reconstruction.
- The novel strategy of diffusing core Gaussians address the feature dilution issues caused by axis-aligned mapping, resulting in a more accurate representation of complex structures.
- Extensive experiments on public datasets have shown that our method is superior to previous methods in terms of visual effects and accurate representation.

2 Related Work

Scene Primitives in Reconstruction. Whether it is a real-world scenario, the human body, or a head, the foundation

of their construction lies in a simple form of scene primitives. Some past approaches have relied on implicit primitives, such as the signed distance function[Wang *et al.*, 2021; Yariv *et al.*, 2023; Yariv *et al.*, 2020; Park *et al.*, 2019; Yariv *et al.*, 2021] that builds objects by tracing points located on the zero-level set of the function in space, or the occupancy function[Mescheder *et al.*, 2019; Zheng *et al.*, 2022; Peng *et al.*, 2020] that represents 3D surfaces as the continuous decision boundaries of deep neural network classifiers. However, these implicit primitives cannot represent complex head avatars. Implicit neural radiance fields[Mildenhall *et al.*, 2021; Gafni *et al.*, 2021; Martin-Brualla *et al.*, 2021] are a way of storing scenes using network weights as primitives, but accompanied by a significant training cost. Explicit scene primitives, such as points[Zheng *et al.*, 2023; Xu *et al.*, 2022], can capture sufficiently complex structures, but due to the fixed shape of points, detailing can only be achieved by continuously refining point radii and increasing point counts during the training process, which introduces significant storage and training overhead.

Here, we use 3D anisotropic Gaussians[Kerbl *et al.*, 2023] as scene primitives. They have deformable shapes, allowing for the representation of intricate details by adjusting their own shapes instead of blindly increasing quantity and reducing radii.

Monocular-video-based Head Portrait Synthesis. The widespread application of head avatars requires convenient capture methods. Some studies[Kirschstein *et al.*, 2023; Teotia *et al.*, 2023] utilize dense multi-view or sparse multi-view to capture dynamic head avatars in space. Although this brings better multi-view consistency, the difficulty of popularizing capture devices hinders the rapid adoption of such technologies. Meanwhile, they mostly reconstruct head dynamics along the temporal axis, sacrificing cross-subject generalization performance. Building head avatars from monocular videos, allowing users to capture data using smartphones, has played a positive role in the promotion of technologies such as virtual reality. Several studies explore the use of monocular data for new view synthesis and high-fidelity reconstruction tasks. They employ implicit surfaces[Zheng *et al.*, 2022; Gafni *et al.*, 2021; Guo *et al.*, 2021], explicit point cloud structures[Zheng *et al.*, 2023], or volumetric neural radiance fields[Xu *et al.*, 2023a; Gao *et al.*, 2022; Tang *et al.*, 2022; Li *et al.*, 2023] as head representations, achieving increasingly realistic visual effects.

Hybrid Neural Field. Previous implicit methods, such as NeRF[Mildenhall *et al.*, 2021], used MLP weights to implicitly represent the scene. This implies that as the complexity of the scene increases, so does the network complexity and learning difficulty. Recently, hybrid neural radiance fields have become a hot topic[Müller *et al.*, 2022; Xu *et al.*, 2023a; Gao *et al.*, 2022; Xu *et al.*, 2023b], storing scenes through explicit data structures (i.e., tri-plane [Chan *et al.*, 2022], hexplane [Cao and Johnson, 2023; Fridovich-Keil *et al.*, 2023], voxel [Müller *et al.*, 2022]) to share the pressure of neural networks, allowing neural networks to focus on decoding semantic information. However, the resolution limitations of explicit structures and the commonly employed axis-aligned mappings can lead to imprecise

representation of features. Our effective Gaussian diffusion strategy successfully addresses the axis-aligned mapping limitations and brings excellent performance to complex regions.

3 Preliminary of 3D Gaussian Splatting

3D gaussian splatting [Kerbl *et al.*, 2023] is an explicit representation method for scenes that utilizes explicit anisotropic 3D Gaussian primitives to represent the underlying structure of the scene. Each 3D Gaussian is an optimizable object with optimizable attributes: position $x \in \mathbb{R}^3$, opacity $\alpha \in \mathbb{R}$, orientation $r \in \mathbb{R}^4$, scaling factor $s \in \mathbb{R}^3$, and spherical harmonic coefficients $Y_{lm} \in \mathbb{R}^k$. For ease of representation, quaternion rotation and scaling factor are merged into the covariance matrix Σ . Therefore, a 3D Gaussian is represented as a 3D Gaussian distribution with a central position μ and a covariance matrix Σ :

$$\mathcal{G}(\mu) = e^{-\frac{1}{2}\mu^T \Sigma^{-1} \mu}, \quad (1)$$

In order to render, 3D Gaussians are arranged above the camera plane and employ a differentiable rasterization technique[Yifan *et al.*, 2019]. The covariance in world space undergoes transformations into the camera coordinate under the changes of the view transformation matrix W and the Jacobian matrix J resulting from affine approximation in the projective transformation[Zwicker *et al.*, 2002; Zwicker *et al.*, 2001]:

$$\Sigma' = JW\Sigma W^T J^T, \quad (2)$$

For each pixel x on the camera plane, the color is synthesized by combining the 3D Gaussians above it:

$$C_x = \sum_{i \in N} c_{i,x} \alpha_{i,x} \prod_{j=1}^{i-1} (1 - \alpha_{j,x}), \quad (3)$$

Where

$$\alpha_{i,x} = \alpha_i e^{-\frac{1}{2}(x-\mu)^T \Sigma^{-1} (x-\mu)}, \quad (4)$$

$c_{i,x}$ is the color of the i -th Gaussian above the pixel. It is calculated using the spherical harmonic coefficients. $\alpha_{i,x}$ represents the opacity of the i -th Gaussian in the region above the pixel x . It is obtained through the center opacity α_i of this Gaussian, its center position μ , and the pixel position x .

4 GaussianHead Method

In the world of space, we randomly initialize 3D Gaussians with positions, orientations, and scales. Conditioned on expression e , through a deformation field, we learn random 3D Gaussians' displacements to the canonical space, denoted as Δ . Multiple sets of learnable quaternions are employed in a diffusion process applied to the core Gaussians within canonical space. The diffused "sub-Gaussians" are subsequently mapped to factor planes, yielding sub-factors. Integration of multiple sub-factors originating from distinct "sub-Gaussians" contributes to the formation of canonical features for the core Gaussians. Decoding is performed based on these canonical features, resulting in opacity α and intermediate latent variables z obtained through the utilization of an opacity MLP M_α . Additionally, the color MLP M_c utilizes both z

and the viewing direction d to generate spherical harmonic coefficients representing view-dependent color. The positions, orientations, scales, opacities, and color attributes of 3D Gaussians are collectively rendered into realistic images through a differentiable rasterizer. Figure. 2 illustrates the workflow of our approach.

4.1 Gaussian Deform Field

3D gaussian splatting is a high-fidelity reconstruction method for static scenes, while head avatars exhibit complex dynamic properties. An approach is to transform dynamic avatars into a canonical space with a common geometric representation. We randomly initialize 3D Gaussians $\mathcal{G}_i = (x_i, r_i, s_i)$ with learnable position x , orientation r , and scale s in world space, where $i = 1, 2, \dots, N$ means the number of 3D Gaussians. Subsequently, we use pre-acquired facial expression parameters e as conditions, employing a deformation multi-layer perceptron to predict position offsets δx , orientation offsets δr , and scale offsets δs based on the initialized 3D Gaussians:

$$(\delta x, \delta r, \delta s) = \mathcal{D}_\theta(\gamma(x), e), \quad (5)$$

Where θ represents the optimized parameters of the deformable MLP, and γ represents the encoding of the spatial coordinates of the 3D Gaussians into a high-dimensional sine-cosine sequence[Mildenhall *et al.*, 2021]. Subsequently, we add offsets onto the initial 3D Gaussians to obtain the canonical Gaussians represented as $\mathcal{G}_o = (x_o, r_o, s_o)$.

4.2 Learnable Gaussian Diffusion

While conventional deformation networks can represent dynamic scenes, a single MLP often struggles to simultaneously capture both dynamic and appearance details due to its limited expressive power and capacity[Kirschstein *et al.*, 2023; Teotia *et al.*, 2023]. Therefore, we propose employing a parametric tri-plane to address the limitations. However, previous works based on explicit tri-plane[Fridovich-Keil *et al.*, 2023; Cao and Johnson, 2023; Chan *et al.*, 2022] have all employed a straightforward fixed axis-aligned mapping to project tracked points onto factor planes, leading to axis-aligned mapping biases[Zhang *et al.*, 2012; Gao *et al.*, 2023]. In more specific terms, primitives located on the same mapping line are redundantly mapped to the same position on the factor plane. This results in the inaccurate updating of the factors stored at those grid points. Moreover, due to the limited resolution of the factor plane, numerous neighboring regions' primitives are mapped to the same resolution grid. As a consequence of the earlier redundant mapping of multiple Gaussians, the factors stored at these grid points are no longer precise, leading to the acquisition of inaccurate features by the primitives in these adjacent regions. We refer to this phenomenon as "feature dilution." This issue is more pronounced in complex structural areas, such as regions obscured by lips, hair, and wrinkles, where there is a greater presence of overlapping.

The prior work[Yi *et al.*, 2023] attempted to address the bias introduced by axis-aligned mapping by simultaneously rotating the entire scene. While effective in static scenarios, shortcomings arise in dynamic scenes. The dynamism inherent in objects disrupts attempts to address misalignments by

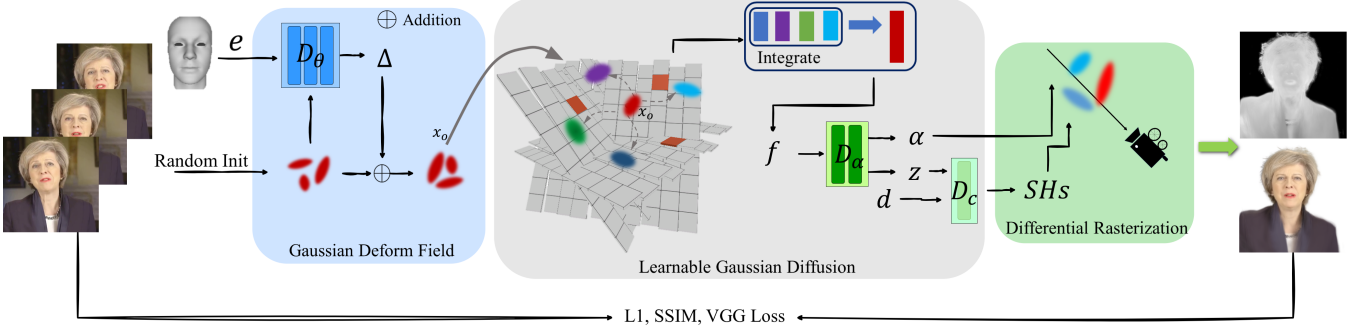


Figure 2: Given a segment of monocular video, we extract camera parameters, RGB frames, expression coefficients, and masks as inputs to our method. The GaussianHead learns the spatial positions, shapes, and sizes of each 3D Gaussian primitive. It combines canonical factors from the explicit dynamic tri-plane to learn the opacity and spherical harmonic coefficients used in differentiable rasterization for image rendering. After training, the GaussianHead can render at a speed of 0.1 seconds per frame.

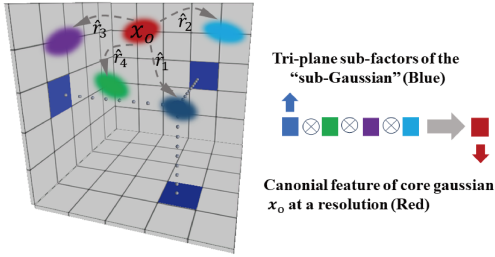


Figure 3: (For simplicity, we only show one quadrant.) The core Gaussian x_o is diffused T times, distorted to T “sub-Gaussians” and further mapped to the factor plane to obtain sub-factors. Multiple sub-factors are combined to form the canonical features of the core Gaussian at a given resolution. For rendering, we still use the position of the core Gaussian x_o instead of the “sub-Gaussians”. Therefore, this process describes the transformation of the original Gaussian features obtained through axis-aligned mappings to canonical features using a learnable mapping to diffuse core Gaussian, referred to as distortions in each entry of the factor plane in Figure. 2.

relying on overall scene rotations. Additionally, this approach proves ineffective in mitigating the issue of feature dilution within overlapping structures.

We parameterize the space tri-plane \mathbf{P}_{xy} , \mathbf{P}_{xz} , \mathbf{P}_{yz} , and set the shape of each plane to (H, W, F) , where H and W represent the size of the plane and F represents the channel number of each factorized plane, encoding geometric and color around the head space.

Each 3D Gaussian \mathcal{G}_o on the canonical space is tracked and generates T sets of rotation vectors to diffuse the 3D Gaussians through random initialization. Directly constructing the rotation vectors as rotation matrices would introduce a significantly increased number of parameters, and optimization for rotation matrices is highly ill-conditioned. Therefore, we propose representing the rotation vectors as unit quaternions $\hat{r} = (a, b_i, c_j, d_k)$, where the number of \hat{r} is equal to T and satisfies $F \bmod T = 0$. In more detail, after processing each quaternion to each rotation vector, we apply the rotation to the core Gaussian to get “sub-Gaussians” and map them to the tri-plane. By bilinear interpolation, we obtain canonical sub-factors \hat{f} (F/T channels). This operation is performed

for T times on one core Gaussian at the same resolution, resulting in T sub-factors they are multiplicatively combined to obtain the canonical features at one resolution (green block in Figure. 3). Finally, we concatenate them across multiple resolutions to obtain the final canonical features f for the core Gaussian \mathcal{G}_o . The above sub-factor multi-resolution integration process proposed by us can be expressed as:

$$f = \bigcup_{r \in \{reso\}} \prod_{i=1}^T \prod_{c=1}^3 \psi_r(\mathbf{P}_c, \hat{r}_i(x_o)), \quad (6)$$

Due to manifold constraints, unit quaternions are restricted to the manifold rather than the entire Euclidean space. Therefore, we employ the Riemannian ADAM optimizer[Béginneul and Ganea, 2018], where updates to unit quaternions induced by the learning rate α_k for the current step k and the loss backward in their tangent space gradient ∇_k ensure adherence to the manifold:

$$\hat{r}_{k+1} = \hat{r}_k \text{Exp}(\alpha_k \nabla_k) \quad (7)$$

4.3 Semantic Information Decoding

In contrast to recent dynamic scene approaches based on 3D Gaussians[Wu *et al.*, 2023; Yang *et al.*, 2023b; Luiten *et al.*, 2023; Yang *et al.*, 2023a] that directly set opacity and color as optimizable parameters, we employ two small MLPs to decode the canonical features into semantic information: opacity α and spherical harmonic coefficients Y_{lm} . This process ensures a more precise generation of opacity and color, as mentioned in Sec. 5.4. Finally, differentiable rasterization in formula.3 is used for rendering.

$$(\alpha, z) = \mathcal{M}_\alpha(f), \quad (8)$$

$$Y_{lm}(\theta, \phi) = \mathcal{M}_c(d, z), \quad (9)$$

Where \mathcal{M}_α and \mathcal{M}_c represent MLPs for decoding opacity and spherical harmonic coefficients, respectively. z and d denote latent variables and view directions, and we use 4th-order spherical harmonic coefficients to synthesize view-dependent colors.



Figure 4: Qualitative comparison with other methods. All methods are run under the configurations specified by their respective authors. Our method has achieved superior visual results, particularly in aspects such as wrinkles, teeth, and even reflections on glasses.

4.4 Inheritance Initialization and T Setting

Unlike a neural radiance field with a constant number of sample points, our Gaussian primitives dynamically increase and decrease with iterations. Therefore, identifying a diffusion strategy that is most congruent with this characteristic is of paramount importance. When a parent Gaussian is clipped into two smaller Gaussians, we employ the diffusion quaternion inherited from the parent Gaussian to diffuse the newly formed smaller Gaussians. Compared to using random or zero initialization, inheritance initialization increases the training speed by approximately 14%, the results are presented in the supplementary materials.

Additionally, the value of T significantly influences training time and the optimal evaluation metrics. We conducted detailed experiments to determine the T , including setting T being set to 2, 4, 8, and 16 to satisfy $F \bmod T = 0$. Additionally, we employed a dynamic T -scheduler that increases T with an increasing number of Gaussians:

$$T = \frac{F}{2^{t-u}}, u = \left\lceil \frac{n_i}{n_o} \right\rceil \quad (10)$$

As the number of 3D Gaussians doubles from the initial

quantity, we increase the T to address potential issues related to the dilution of features. Where F is the number of feature channels, n_i is the current number of Gaussians, n_o is the initialized number of Gaussians, and t is a constant, we have set it to 6. The results of the T experiment are shown in Figure. 6. In the context of a fixed T , an excessively large T introduces optimization challenges, notably evidenced by a pronounced deceleration in the optimization process at $T = 8$ and 16. Conversely, a T that is too small proves inadequate in addressing the issue of feature dilution, leading to a discernible deterioration in metrics. The incorporation of a T -scheduler did not yield superior outcomes, attributed in part to the predominant occurrence of newly introduced Gaussians in vacant regions. These regions, in contrast to their densely optimized counterparts, contribute minimally to the likelihood of feature dilution.

4.5 Training Objectives

We utilize L1 loss is employed to measure the pixel-wise difference, perceptual loss and D-SSIM loss to measure the quality loss of the rendered images.

$$\mathcal{L}_{\text{rgb}} = \|\mathbf{I} - \mathbf{I}^{\text{GT}}\|_1, \quad (11)$$

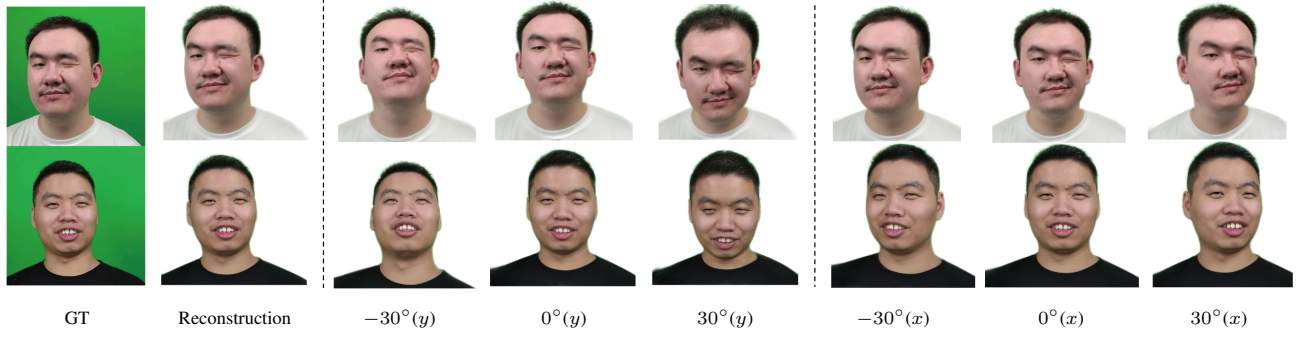


Figure 5: Novel view synthesis results of GaussianHead: we rotate the camera viewpoint around the x and y axes to acquire a novel view. In these novel perspectives, there is a pronounced consistency in representing details such as teeth, wrinkles, and hair.

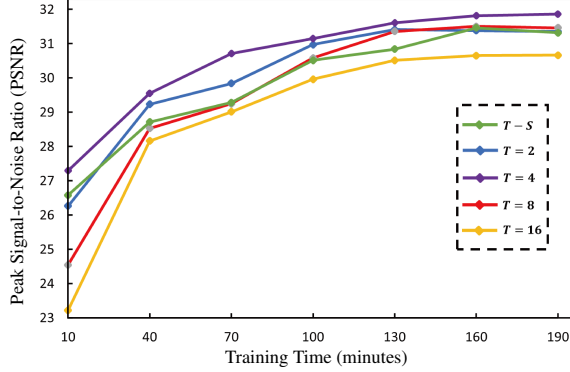


Figure 6: The performance of various values of T during the training process (“ $T - S$ ” in the figure represents the T -scheduler). Optimal performance was achieved when T was set to 4 in our task.

$$\mathcal{L}_{\text{vgg}} = \|\text{vgg}(\mathbf{I}) - \text{vgg}(\mathbf{I}^{\text{GT}})\|_1, \quad (12)$$

$$\mathcal{L}_{\text{D-ssim}} = 1 - \text{ssim}(\mathbf{I}, \mathbf{I}^{\text{GT}}), \quad (13)$$

Method	L1↓	PSNR↑	SSIM↑	LPIPS↓
INSTA[Zielonka <i>et al.</i> , 2023]	0.00182	27.41	0.892	0.141
NeRFBlendShape[Gao <i>et al.</i> , 2022]	0.00117	29.32	0.911	0.102
PointAvatar[Zheng <i>et al.</i> , 2023]	0.00211	26.76	0.8611	0.162
GaussianHead(Ours)	0.00067	31.85	0.940	0.091

Table 2: In comparison regarding the accuracy of reconstruction: Our GaussianHead has made significant strides, achieving superior quality results over baseline methods.

5 Experiments

5.1 Baselines

We choose relatively state-of-the-art head avatar methods: INSTA[Zielonka *et al.*, 2023] based on volumetric NeRF, reconstructs avatars by building a neural surface on the foundation of 3DMM; PointAvatar[Zheng *et al.*, 2023] based on explicit points, constructs detailed avatars using iteratively refined and upsampled point clouds. NeRFBlendShape[Gao *et al.*

et al., 2022] based on hybrid NeRF, utilizes a hash grid as the storage structure for the facial expression base to construct high-fidelity head avatars.

5.2 Qualitative and Quantitative Comparison in Reconstruction

We showcase our excellent visual quality in Figure. 4 and supplementary materials. PointAvatar[Zheng *et al.*, 2023] reconstructs avatars based on explicit points, however, expression movements controlled by linear blend skinning (LBS) fail to capture extreme expressions. Furthermore, based on fixed-shaped points, it is very easy for reconstruction holes to occur. NerfBlendshape[Gao *et al.*, 2022], which employs an explicit hash table to store features, but due to the resolution limitations, it is prone to producing a blurry and smoothing effect, making it difficult to express realistic textures. INSTA[Zielonka *et al.*, 2023] builds instant neural primitives on the FLAME model and employs geometric regularization from a 3DMM-driven dynamic density field to construct the head. This is constrained not only by the resolution of neural primitives but also by the limitations of the 3DMM-driven components. Meanwhile, all of the above methods come with a strong smoothing effect. From a visual perspective, we are able to effectively represent subtle details such as slightly closed eyes and wrinkles. Even with only a few frames featuring the oral cavity in a training dataset comprising thousands of frames, we can achieve precise reconstruction (refer to Figure. 9). This is something that previous methods based on monocular video for head avatars were unable to accomplish. We report the results of quantitative comparisons in Table. 2.

5.3 Novel View Synthesis and Cross-Identity Reenactment

The generated avatars by GaussianHead exhibit excellent multi-view consistency, as illustrated in Figure. 5. The results show no artifacts or unrealistic facial expressions, even at intermediate rotation angles. At the same time, our method can also accurately represent details, such as teeth, from novel perspectives. Furthermore, we conducted a comparative study in the context of cross-identity reenactment with other methods. GaussianHead excels in faithfully facilitating motion control by other subjects. Our approach demonstrates

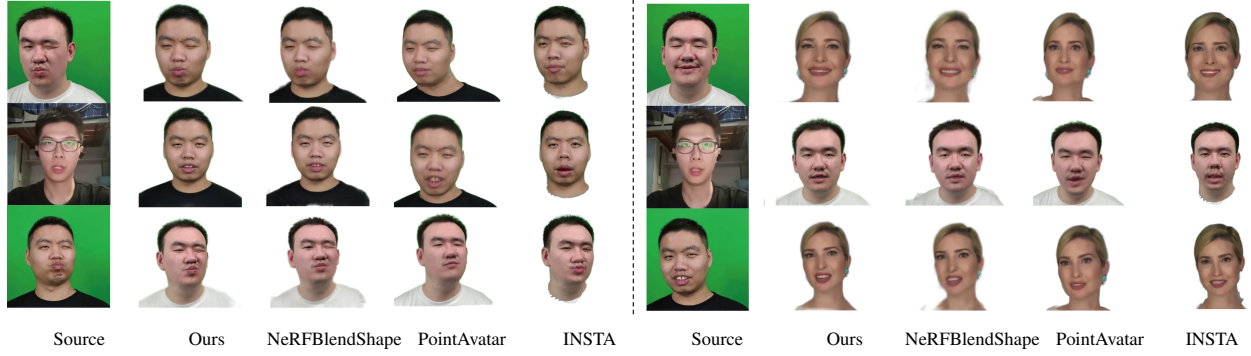


Figure 7: We use the source subject to drive the execution of new poses and expressions for the reconstructed avatars and conduct cross-method comparisons. Our method achieves the best reenactment results, even successfully conveying extreme expressions.

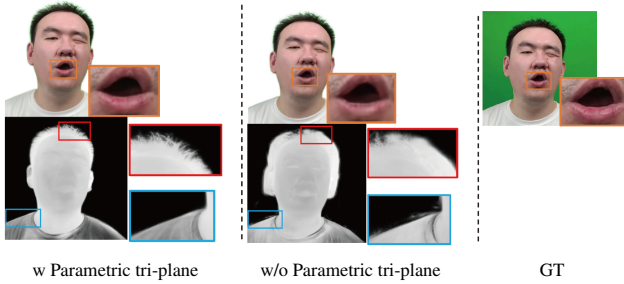


Figure 8: We melted down the results of parameterized tri-plane and observed that a single-deformation MLP is unable to learn precise Gaussian attributes for rendering.

outstanding performance in this task, particularly in the reenactment of extreme facial expressions. For example, the first and third rows on the left side of Figure. 7.

5.4 Ablation studies

Parametric tri-plane. Due to limitations in the capacity and expressive power of a single MLP, it is challenging to simultaneously capture the dynamic facial muscle movements and textures. We introduce parametric tri-plane as an additional component, where a multi-resolution grid representation is crucial for achieving high-detail representation[Müller *et al.*, 2022]. We ablate the parametric tri-plane, directly optimizing the opacity and spherical harmonic coefficients of dynamic 3D Gaussians as trainable parameters. We present the ablation results in Figure. 8. The depth maps we visualize reveal numerous Gaussians around the head that are not eliminated through cropping, indicating the limitations of a single MLP in accurately learning opacity, the presence of these meaningless Gaussians can somewhat increase training overhead and the perceptual negative impacts.

Learnable Gaussian Diffusion. Almost all methods that utilized explicit feature container in the past have followed the practice of tracing 3D coordinates in space and directly mapping them to a two-dimensional plane or a three-dimensional voxel grid through axis-aligned means, which can introduce biases in the final results[Zhang *et al.*, 2012; Yi *et al.*, 2023], and it will clearly lead to the dilution of

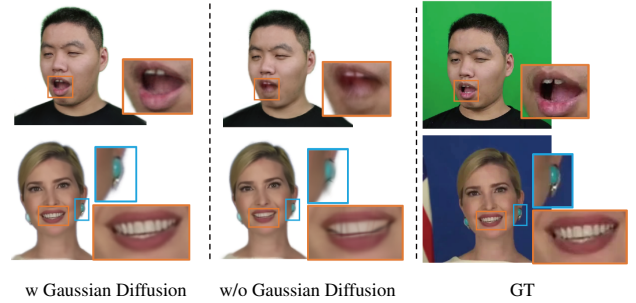


Figure 9: The novel Gaussian diffusion strategy accurately restores features representing various complex regions, enabling the rendering of high-fidelity details even for rarely seen oral cavity in the training data.

	L1↓	PSNR↑	SSIM↑	LPIPS↓
w/o Parametric Tri-plane	0.00090	30.47	0.891	0.144
w/o Gaussian Diffusion	0.00073	31.35	0.912	0.115
Ours Full	0.00067	31.85	0.940	0.091

Table 3: We systematically ablated several key components and assessed quantitative performance to demonstrate their effectiveness.

features in different regions. In GaussianHead, we employ learnable Gaussian diffusion by introducing a set of quaternion quaternions that controls the process. This allows the tracked 3D coordinates to find the optimal grid factor, resulting in finer details. We conducted ablation experiments using a fixed mapping approach like[Fridovich-Keil *et al.*, 2023; Chan *et al.*, 2022] and referred to as “w/o Gaussian Diffusion” in Figure. 9 and Table. 3.

6 Conclusion

We propose GaussianHead: a realistic avatar generation algorithm based on 3D Gaussians with learnable diffusion. We use 3D Gaussians as efficient and accurate scene primitives, obtaining features on the tri-plane through multiple diffusions of 3D Gaussians in canonical space. By employing a novel factor fusion approach, we achieve accurate features capable of faithfully reproducing various details, such as teeth, wrin-

kles, and even pores. Finally, we leverage efficient differentiable rasterization to render impressive results for tasks like self-reconstruction, cross-identity driving, and novel perspective synthesis.

7 Appendix

In the supplementary materials, we first provide a detailed overview of our network architecture and parameter settings, following the experimental results showcased, including error maps and depth maps. Finally, there are experiments on determining the initialization scheme.

A Implementation Details

A.1 Dataset Acquisition

In order to facilitate a fair comparison among all methods, all our data is sourced from an open dataset[Gao *et al.*, 2022]. The training data for each subject comprises approximately 2000 to 2500 frames, and the evaluation is conducted using the last 3% to 5% frames. Specifically, the data for each subject we used only includes four parts: RGB head images, expression parameters (derived from 3DMM model fitting[Gerig *et al.*, 2018; Li *et al.*, 2017]), camera parameters, and binary masks (the first three sections are all from open datasets, and the binary masks are created using MODNet[Ke *et al.*, 2022]).

A.2 Hyperparameter Configuration

We implemented GaussianHead with PyTorch, where differentiable 3D Gaussian rasterization is implemented based on CUDA kernels[Kerbl *et al.*, 2023]. The initialization includes 10K 3D Gaussians. Apart from optimizing the manifold using Riemannian ADAM[Bécigneul and Ganea, 2018], all other optimizers use first-order ADAM[Kingma and Ba, 2014], and a linear learning rate scheduler is applied. In our experiments, we set the batch size to 1 and trained for 80k iterations (about 30 epochs) on a single RTX 3090, taking approximately 3 hours.

After 3000 iterations, we perform densification of 3D Gaussians and clipping of overly large Gaussians with very low opacity every 500 iterations. We set the opacity threshold to 0.0002 and the size threshold for large Gaussians to be greater than 1% of the scene. Other details follow the settings in[Kerbl *et al.*, 2023].

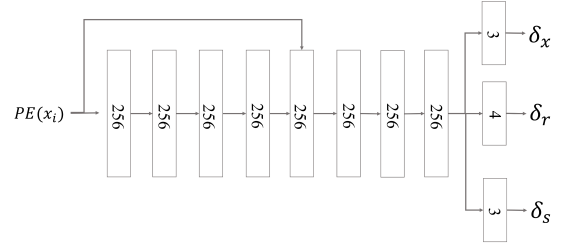
Our loss function includes rgb loss \mathcal{L}_{rgb} , perceptual loss \mathcal{L}_{vgg} , and D-SSIM loss $\mathcal{L}_{\text{D-ssim}}$. Here, we employ the first four layers of the VGG model[Simonyan and Zisserman, 2014] to assess the similarity between the intermediate layer features of rendered images and real images, aiming to derive the perceptual loss. The final loss function is as follows:

$$\mathcal{L} = \lambda_1 \mathcal{L}_{\text{rgb}} + \lambda_2 \mathcal{L}_{\text{vgg}} + \lambda_3 \mathcal{L}_{\text{D-ssim}} \quad (14)$$

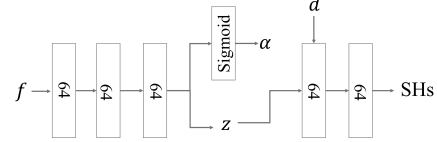
We set $\lambda_1 = 0.8$, $\lambda_2 = 0.01$, $\lambda_3 = 0.2$.

A.3 Network Configuration

The network architecture is shown in Figure. 10. Our main optimization parameters include a deformable multi-layer perceptron, parameterized tri-plane, and a quaternion



(a) Deform Network



(b) Semantic Decoder Network

Figure 10: Our network architecture diagram provides a detailed overview of the network layers, width, and data flow. Specific network parameter configurations are elaborated in appendix.

group T used to transform the traced Gaussians into “aligned Gaussians.” We use positional encoding with a frequency of 10 for the initial Gaussians x_i in the input deformation network. The deformable network consists of 8 linear layers with a width of 256, and skip connections are added in the fourth layer. After the eighth linear layer, three output heads, respectively, output the position, rotation, and scale offsets of the 3D Gaussians. all of which are activated using ReLU. We set the learning rate for 3D Gaussian position to 1.6×10^{-4} , linearly decaying to 1.6×10^{-6} over training steps; rotation and scale have a learning rate of 1×10^{-3} .

We initialize the parameters of the multi-resolution tri-plane with a uniform distribution in the range $[0.1, 0.5]$. The base resolution is set to 64 and is multiplied by super-resolution scales: 1, 2, 4, 8, resulting in the final four resolutions. For the canonical factors obtained from the tri-plane, we use an opacity network with a width of 64 and 3 layers to process them. The opacity and intermediate variables’ outputs are activated by the sigmoid. The variables are concatenated with the view direction and fed into a color network with a depth of 2 and a width of 64. The ReLU is used for activation to obtain spherical harmonic coefficients. The learning rate for the parameterized grid is 1×10^{-3} , linearly decaying to 0 at the last iteration; the opacity parameter learning rate is 1×10^{-4} . For learning the spherical harmonic coefficients representing color, the learning rate for the first-order coefficient is 1×10^{-3} , and for the subsequent three-order coefficients, it is 5×10^{-5} .

Regarding the quaternion group T controlling Gaussian distortions, we treat them as trainable parameters, initializing them with random numbers in the range $[0, 2^{32}]$, uniformly distributing them on a four-dimensional sphere as initial quaternions. Their learning rate decays from 1×10^{-3} to 0 at the last iteration.

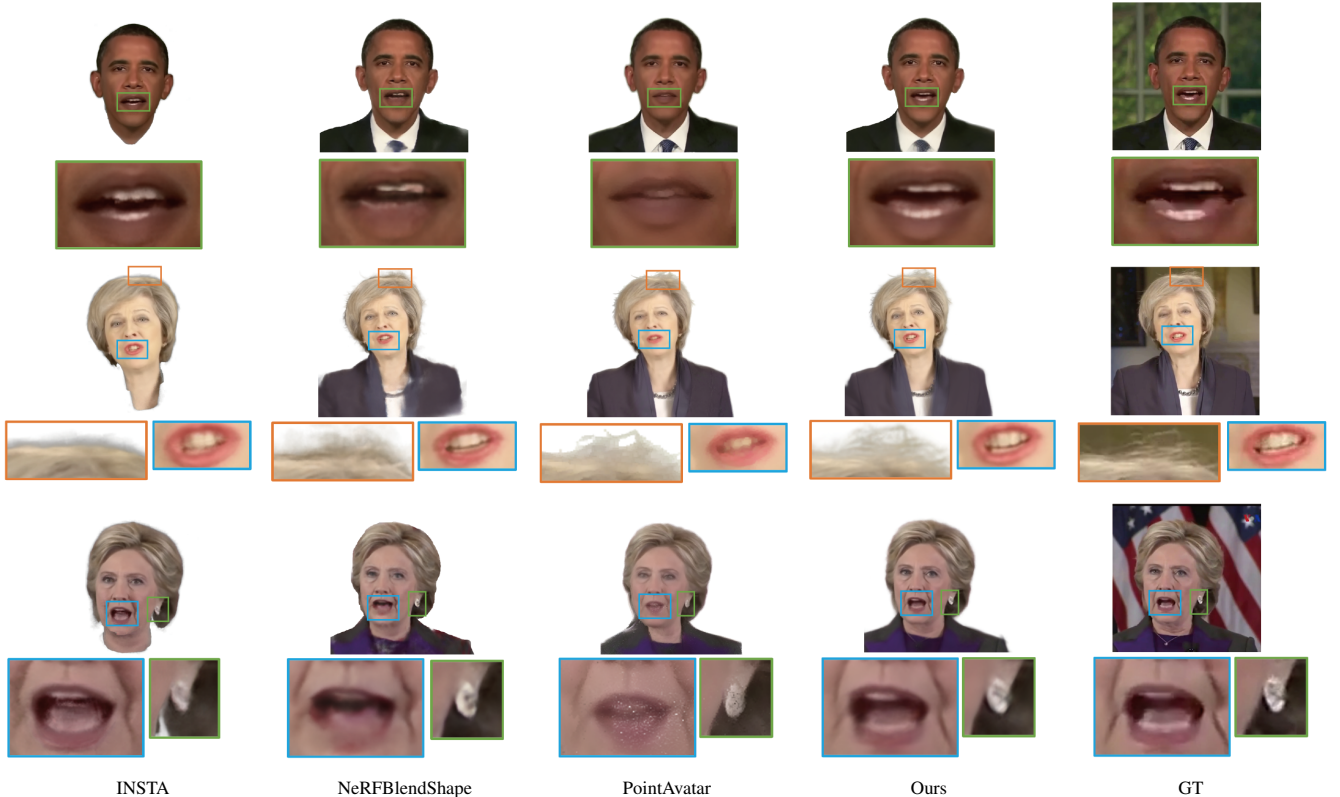


Figure 11: In comparison with other subjects, our approach continues to demonstrate superior performance in both overall quality and finer details. For instance, it excels in capturing subtle elements such as individual strands of hair suspended above the head and intricate internal structures like the oral cavity.

	Inheritance Initialization	Random Initialization	Zero Initialization
Training Time (minutes)	180	210	208

Table 4: The optimization time required to achieve the optimal metrics for the three diffusion quaternions initialization methods.

B More Results

B.1 Comparison of Other Subjects

We conducted experiments comparing with other subjects, and the experimental results are visible in Figure. 11.

B.2 Comparison of Error Maps

The error map, as opposed to the RGB image, can more clearly reflect the reconstruction accuracy. We calculated the L1 distance between the reconstructed images and ground truth on a per-pixel basis, and mapped this information to the color space to generate the final error map. We compared this aspect with INSTA[Zielonka *et al.*, 2023], NeRFBlendShape[Gao *et al.*, 2022] and PointAvatar[Zheng *et al.*, 2023], the results are presented in Figure. 12.

B.3 Accurate Depth Estimation

We additionally present the reconstructed precise depth map results in Figure. 13, from which it can be clearly seen

whether there is the presence of artifacts. Our method demonstrates excellent depth effects.

C Parameter Experiments

C.1 Initialization Diffusion Quaternions

In the neural radiance field[Mildenhall *et al.*, 2021], the number of sampled points in the scene is mostly fixed. However, our GaussianHead undergoes densification of 3D Gaussians as the iterations progress. For the 3D Gaussians that are clipped out, we directly delete their quaternions used for controlling diffusion. However, for the newly added 3D Gaussians that split from the parent Gaussian, we evaluated three initialization schemes for diffusion quaternions: randomly initializing from the range $[0, 2^{32}]$ as done at the beginning of training, inheriting diffusion parameters from the parent Gaussian, and zero initialization. We compared the time required for these three approaches to achieve the optimal metrics of GaussianHead in the table. 4. Inheriting initialization helps avoid optimizing diffusion parameters randomly or initializing them to zero from scratch, further reducing training time.

D Limitation

GaussianHead achieves high-fidelity reconstruction of head avatars with superior generalization performance in motion.

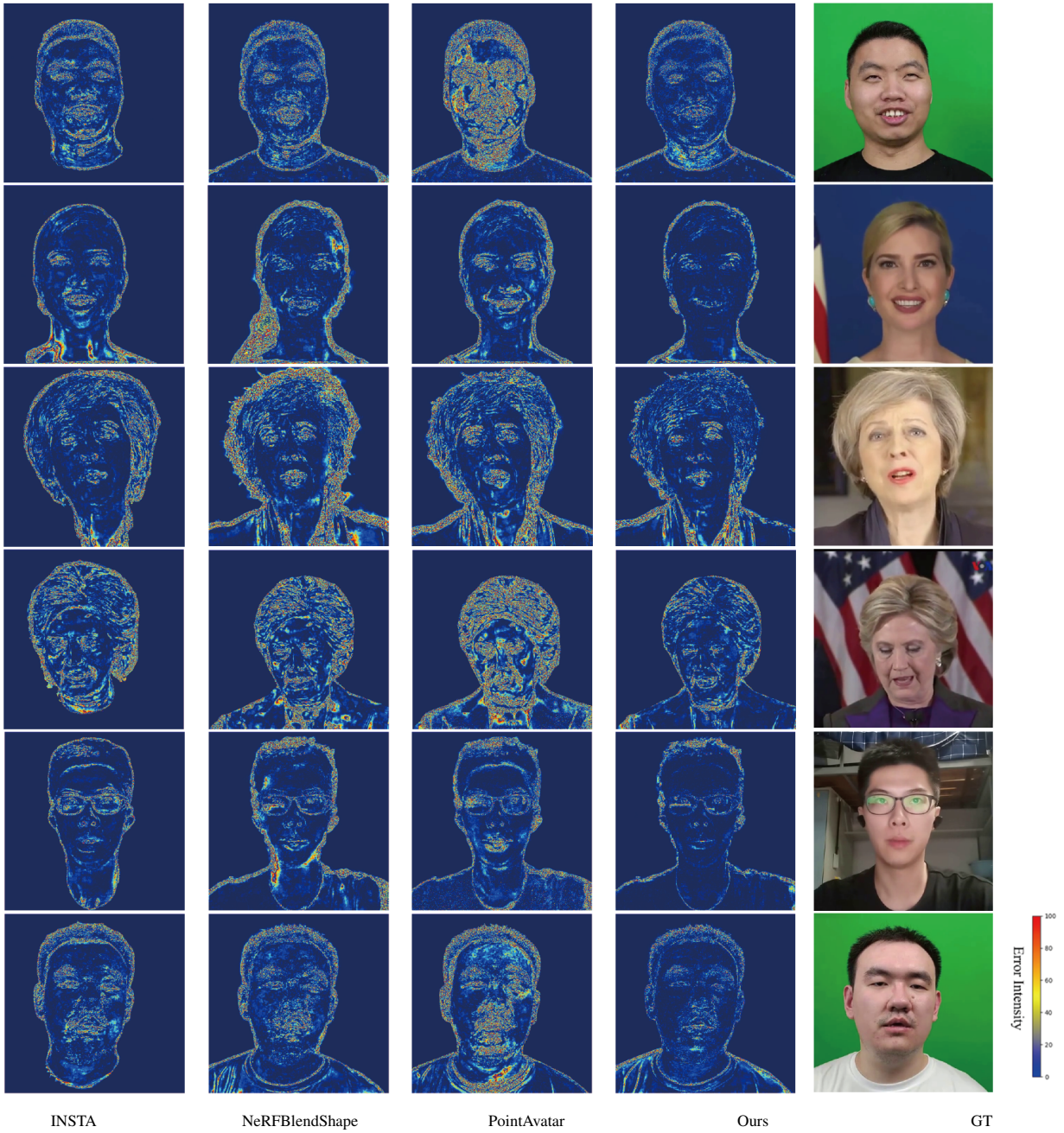


Figure 12: In comparison with INSTA, NeRFBlendShape, and PointAvatar on the error map, our approach exhibits the overall minimum reconstruction error, showcasing the highest quality of reconstruction.



Figure 13: We reconstruct the ground truth image (left) into a head avatar (center) and simultaneously visualize the depth estimated by GaussianHead (right). Our method obtains accurate depth information.

However, our method currently encompasses only the shoulders and above. For accurate emotional expression, consideration of reconstructing the complete upper body, including hand gestures, is crucial. Therefore, the reconstruction of the entire upper body and hand limbs holds significant importance for generating digitally rendered portraits with enhanced emotional expressiveness.

Furthermore, our method does not separate the motion of the head and torso. Existing separation methods either utilize semantic masks for independent training of the head and torso [Guo et al., 2021; Tang et al., 2022; Li et al., 2023] or explicitly control their motion separately using the LBS algorithm of 3DMM [Zheng et al., 2022; Zheng et al., 2023]. The former complicates the entire training process and cannot achieve end-to-end training. The latter, although capable of separately controlling the broad-range pose movements of the head and torso, exhibits poor performance in controlling subtle expressions; most complex expressions are challenging to articulate. Therefore, investigating a prospective and practical end-to-end method that achieves partial structural separation control while efficiently expressing subtle facial expressions is a promising avenue and a focus of our future work.

References

- [Bécigneul and Ganea, 2018] Gary Bécigneul and Octavian-Eugen Ganea. Riemannian adaptive optimization methods. *arXiv preprint arXiv:1810.00760*, 2018.
- [Cao and Johnson, 2023] Ang Cao and Justin Johnson. Hexplane: A fast representation for dynamic scenes. In *Proceedings of the IEEE/CVF Conference on Computer Vision and Pattern Recognition*, pages 130–141, 2023.
- [Cao et al., 2013] Chen Cao, Yanlin Weng, Shun Zhou, Yiyong Tong, and Kun Zhou. Facewarehouse: A 3d facial expression database for visual computing. *IEEE Transactions on Visualization and Computer Graphics*, 20(3):413–425, 2013.
- [Chan et al., 2022] Eric R Chan, Connor Z Lin, Matthew A Chan, Koki Nagano, Boxiao Pan, Shalini De Mello, Orazio Gallo, Leonidas J Guibas, Jonathan Tremblay, Sameh Khamis, et al. Efficient geometry-aware 3d generative adversarial networks. In *Proceedings of the IEEE/CVF Conference on Computer Vision and Pattern Recognition*, pages 16123–16133, 2022.
- [Chen et al., 2022] Anpei Chen, Zexiang Xu, Andreas Geiger, Jingyi Yu, and Hao Su. Tensorf: Tensorial radiance fields. In *European Conference on Computer Vision*, pages 333–350. Springer, 2022.
- [Fridovich-Keil et al., 2023] Sara Fridovich-Keil, Giacomo Meanti, Frederik Rahbæk Warburg, Benjamin Recht, and Angjoo Kanazawa. K-planes: Explicit radiance fields in space, time, and appearance. In *Proceedings of the IEEE/CVF Conference on Computer Vision and Pattern Recognition*, pages 12479–12488, 2023.
- [Gafni et al., 2021] Guy Gafni, Justus Thies, Michael Zollhofer, and Matthias Nießner. Dynamic neural radiance fields for monocular 4d facial avatar reconstruction. In *Proceedings of the IEEE/CVF Conference on Computer Vision and Pattern Recognition*, pages 8649–8658, 2021.
- [Gao et al., 2022] Xuan Gao, Chenglai Zhong, Jun Xiang, Yang Hong, Yudong Guo, and Juyong Zhang. Reconstructing personalized semantic facial nerf models from monocular video. *ACM Transactions on Graphics (TOG)*, 41(6):1–12, 2022.
- [Gao et al., 2023] Quankai Gao, Qiangeng Xu, Hao Su, Ulrich Neumann, and Zexiang Xu. Strivec: Sparse tri-vector radiance fields. In *Proceedings of the IEEE/CVF International Conference on Computer Vision*, pages 17569–17579, 2023.
- [Gerig et al., 2018] Thomas Gerig, Andreas Morel-Forster, Clemens Blumer, Bernhard Egger, Marcel Luthi, Sandro Schönborn, and Thomas Vetter. Morphable face models—an open framework. In *2018 13th IEEE International Conference on Automatic Face & Gesture Recognition (FG 2018)*, pages 75–82. IEEE, 2018.
- [Guo et al., 2021] Yudong Guo, Keyu Chen, Sen Liang, Yongjin Liu, Hujun Bao, and Juyong Zhang. Ad-nerf: Audio driven neural radiance fields for talking head synthesis. In *IEEE/CVF International Conference on Computer Vision (ICCV)*, 2021.

- [Ke *et al.*, 2022] Zhanghan Ke, Jiayu Sun, Kaican Li, Qiong Yan, and Rynson WH Lau. Modnet: Real-time trimap-free portrait matting via objective decomposition. In *Proceedings of the AAAI Conference on Artificial Intelligence*, volume 36, pages 1140–1147, 2022.
- [Kerbl *et al.*, 2023] Bernhard Kerbl, Georgios Kopanas, Thomas Leimkühler, and George Drettakis. 3d gaussian splatting for real-time radiance field rendering. *ACM Transactions on Graphics (ToG)*, 42(4):1–14, 2023.
- [Kingma and Ba, 2014] Diederik P Kingma and Jimmy Ba. Adam: A method for stochastic optimization. *arXiv preprint arXiv:1412.6980*, 2014.
- [Kirschstein *et al.*, 2023] Tobias Kirschstein, Shenhan Qian, Simon Giebenhain, Tim Walter, and Matthias Nießner. Nersemble: Multi-view radiance field reconstruction of human heads. *arXiv preprint arXiv:2305.03027*, 2023.
- [Li *et al.*, 2017] Tianye Li, Timo Bolkart, Michael J Black, Hao Li, and Javier Romero. Learning a model of facial shape and expression from 4d scans. *ACM Trans. Graph.*, 36(6):194–1, 2017.
- [Li *et al.*, 2023] Jiahe Li, Jiawei Zhang, Xiao Bai, Jun Zhou, and Lin Gu. Efficient region-aware neural radiance fields for high-fidelity talking portrait synthesis. In *Proceedings of the IEEE/CVF International Conference on Computer Vision*, pages 7568–7578, 2023.
- [Luiten *et al.*, 2023] Jonathon Luiten, Georgios Kopanas, Bastian Leibe, and Deva Ramanan. Dynamic 3d gaussians: Tracking by persistent dynamic view synthesis. *arXiv preprint arXiv:2308.09713*, 2023.
- [Martin-Brualla *et al.*, 2021] Ricardo Martin-Brualla, Noha Radwan, Mehdi SM Sajjadi, Jonathan T Barron, Alexey Dosovitskiy, and Daniel Duckworth. Nerf in the wild: Neural radiance fields for unconstrained photo collections. In *Proceedings of the IEEE/CVF Conference on Computer Vision and Pattern Recognition*, pages 7210–7219, 2021.
- [Mescheder *et al.*, 2019] Lars Mescheder, Michael Oechsle, Michael Niemeyer, Sebastian Nowozin, and Andreas Geiger. Occupancy networks: Learning 3d reconstruction in function space. In *Proceedings of the IEEE/CVF conference on computer vision and pattern recognition*, pages 4460–4470, 2019.
- [Mildenhall *et al.*, 2021] Ben Mildenhall, Pratul P Srinivasan, Matthew Tancik, Jonathan T Barron, Ravi Ramamoorthi, and Ren Ng. Nerf: Representing scenes as neural radiance fields for view synthesis. *Communications of the ACM*, 65(1):99–106, 2021.
- [Müller *et al.*, 2022] Thomas Müller, Alex Evans, Christoph Schied, and Alexander Keller. Instant neural graphics primitives with a multiresolution hash encoding. *ACM Transactions on Graphics (ToG)*, 41(4):1–15, 2022.
- [Park *et al.*, 2019] Jeong Joon Park, Peter Florence, Julian Straub, Richard Newcombe, and Steven Lovegrove. Deepsdf: Learning continuous signed distance functions for shape representation. In *Proceedings of the IEEE/CVF conference on computer vision and pattern recognition*, pages 165–174, 2019.
- [Peng *et al.*, 2020] Songyou Peng, Michael Niemeyer, Lars Mescheder, Marc Pollefeys, and Andreas Geiger. Convolutional occupancy networks. In *Computer Vision–ECCV 2020: 16th European Conference, Glasgow, UK, August 23–28, 2020, Proceedings, Part III 16*, pages 523–540. Springer, 2020.
- [Simonyan and Zisserman, 2014] Karen Simonyan and Andrew Zisserman. Very deep convolutional networks for large-scale image recognition. *arXiv preprint arXiv:1409.1556*, 2014.
- [Tang *et al.*, 2022] Jiaxiang Tang, Kaisiyuan Wang, Hang Zhou, Xiaokang Chen, Dongliang He, Tianshu Hu, Jingtuo Liu, Gang Zeng, and Jingdong Wang. Real-time neural radiance talking portrait synthesis via audio-spatial decomposition. *arXiv preprint arXiv:2211.12368*, 2022.
- [Teotia *et al.*, 2023] Kartik Teotia, Xingang Pan, Hyeonwoo Kim, Pablo Garrido, Mohamed Elgharib, Christian Theobalt, et al. Hq3davatar: High quality controllable 3d head avatar. *arXiv preprint arXiv:2303.14471*, 2023.
- [Wang *et al.*, 2021] Peng Wang, Lingjie Liu, Yuan Liu, Christian Theobalt, Taku Komura, and Wenping Wang. Neus: Learning neural implicit surfaces by volume rendering for multi-view reconstruction. *arXiv preprint arXiv:2106.10689*, 2021.
- [Wu *et al.*, 2023] Guanjun Wu, Taoran Yi, Jiemin Fang, Lingxi Xie, Xiaopeng Zhang, Wei Wei, Wenyu Liu, Qi Tian, and Xinggang Wang. 4d gaussian splatting for real-time dynamic scene rendering. *arXiv preprint arXiv:2310.08528*, 2023.
- [Xu *et al.*, 2022] Qiangeng Xu, Zexiang Xu, Julien Philip, Sai Bi, Zhixin Shu, Kalyan Sunkavalli, and Ulrich Neumann. Point-nerf: Point-based neural radiance fields. In *Proceedings of the IEEE/CVF Conference on Computer Vision and Pattern Recognition*, pages 5438–5448, 2022.
- [Xu *et al.*, 2023a] Yuelang Xu, Lizhen Wang, Xiaochen Zhao, Hongwen Zhang, and Yebin Liu. Avatarmav: Fast 3d head avatar reconstruction using motion-aware neural voxels. In *ACM SIGGRAPH 2023 Conference Proceedings*, pages 1–10, 2023.
- [Xu *et al.*, 2023b] Yuelang Xu, Hongwen Zhang, Lizhen Wang, Xiaochen Zhao, Han Huang, Guojun Qi, and Yebin Liu. Latentavatar: Learning latent expression code for expressive neural head avatar. *arXiv preprint arXiv:2305.01190*, 2023.
- [Yang *et al.*, 2023a] Zeyu Yang, Hongye Yang, Zijie Pan, Xiatian Zhu, and Li Zhang. Real-time photorealistic dynamic scene representation and rendering with 4d gaussian splatting. *arXiv preprint arXiv:2310.10642*, 2023.
- [Yang *et al.*, 2023b] Ziyi Yang, Xinyu Gao, Wen Zhou, Shaohui Jiao, Yuqing Zhang, and Xiaogang Jin. Deformable 3d gaussians for high-fidelity monocular dynamic scene reconstruction. *arXiv preprint arXiv:2309.13101*, 2023.
- [Yariv *et al.*, 2020] Lior Yariv, Yoni Kasten, Dror Moran, Meirav Galun, Matan Atzmon, Basri Ronen, and Yaron

- Lipman. Multiview neural surface reconstruction by disentangling geometry and appearance. *Advances in Neural Information Processing Systems*, 33:2492–2502, 2020.
- [Yariv *et al.*, 2021] Lior Yariv, Jiatao Gu, Yoni Kasten, and Yaron Lipman. Volume rendering of neural implicit surfaces. *Advances in Neural Information Processing Systems*, 34:4805–4815, 2021.
- [Yariv *et al.*, 2023] Lior Yariv, Peter Hedman, Christian Reiser, Dor Verbin, Pratul P Srinivasan, Richard Szeliski, Jonathan T Barron, and Ben Mildenhall. Baked sdf: Meshing neural sdfs for real-time view synthesis. *arXiv preprint arXiv:2302.14859*, 2023.
- [Yi *et al.*, 2023] Brent Yi, Weijia Zeng, Sam Buchanan, and Yi Ma. Canonical factors for hybrid neural fields. In *Proceedings of the IEEE/CVF International Conference on Computer Vision*, pages 3414–3426, 2023.
- [Yifan *et al.*, 2019] Wang Yifan, Felice Serena, Shihao Wu, Cengiz Öztireli, and Olga Sorkine-Hornung. Differentiable surface splatting for point-based geometry processing. *ACM Transactions on Graphics (TOG)*, 38(6):1–14, 2019.
- [Zhang *et al.*, 2012] Zhengdong Zhang, Arvind Ganesh, Xiao Liang, and Yi Ma. Tilt: Transform invariant low-rank textures. *International journal of computer vision*, 99:1–24, 2012.
- [Zheng *et al.*, 2022] Yufeng Zheng, Victoria Fernández Abrevaya, Marcel C Bühler, Xu Chen, Michael J Black, and Otmar Hilliges. Im avatar: Implicit morphable head avatars from videos. In *Proceedings of the IEEE/CVF Conference on Computer Vision and Pattern Recognition*, pages 13545–13555, 2022.
- [Zheng *et al.*, 2023] Yufeng Zheng, Wang Yifan, Gordon Wetzstein, Michael J Black, and Otmar Hilliges. Pointavatar: Deformable point-based head avatars from videos. In *Proceedings of the IEEE/CVF Conference on Computer Vision and Pattern Recognition*, pages 21057–21067, 2023.
- [Zielonka *et al.*, 2023] Wojciech Zielonka, Timo Bolkart, and Justus Thies. Instant volumetric head avatars. In *Proceedings of the IEEE/CVF Conference on Computer Vision and Pattern Recognition*, pages 4574–4584, 2023.
- [Zwicker *et al.*, 2001] Matthias Zwicker, Hanspeter Pfister, Jeroen Van Baar, and Markus Gross. Surface splatting. In *Proceedings of the 28th annual conference on Computer graphics and interactive techniques*, pages 371–378, 2001.
- [Zwicker *et al.*, 2002] Matthias Zwicker, Hanspeter Pfister, Jeroen Van Baar, and Markus Gross. Ewa splatting. *IEEE Transactions on Visualization and Computer Graphics*, 8(3):223–238, 2002.